INTERNATIONAL JOURNAL FOR NUMERICAL METHODS IN FLUIDS, VOL. 13, 999–1028 (1991)

LARGE-SCALE COMPUTER SIMULATION OF FULLY DEVELOPED TURBULENT CHANNEL FLOW WITH HEAT TRANSFER

STEPHEN L. LYONS* AND THOMAS J. HANRATTY

Department of Chemical Engineering, University of Illinois, Urbana, IL 61801, U.S.A.

AND

JOHN B. McLAUGHLIN

Department of Chemical Engineering, Clarkson University, Potsdam, NY 13676, U.S.A.

SUMMARY

Recently, with the advent of supercomputers, there has been considerable interest in the use of direct numerical simulation to obtain information about turbulent shear flow at low Reynolds number. This paper presents a pseudospectral technique to solve the full three-dimensional time-dependent Navier–Stokes and advection–diffusion equations without the use of subgrid-scale modelling. The technique has not been previously used for fully developed turbulent channel flow simulation and is based on methods applied in other contexts. The emphasis of this paper is to provide a reasonably detailed account of how the simulation is done rather than to present new calculations of turbulence. The details of an algorithm for turbulent channel flow simulation and the grid and time step sizes needed to integrate through transient behaviour to steady state turbulence have not been published before and are presented here.

Results from a Cray-2 simulation of fully developed turbulent flow in a channel with heat transfer are presented along with a critical comparison between experiment and computation. The first- and second-order moments agree well with experimental measurements; the agreement is poor for higher-order moments such as the skewness and flatness near the walls of the channel. Detailed information given about the effects of spatial grid resolution on a computed results is important for estimating the size of the computation required to study various aspects of a turbulent flow.

KEY WORDS Turbulence Channel Heat transfer Spectral Numerical Simulation

1. INTRODUCTION

The principal theoretical problems of wall turbulence are to determine how turbulence is generated and sustained and to relate transport of momentum and scalar quantities to the fluctuating velocity field. In recent years considerable attention has been given to the discovery that turbulent flow in the viscous wall layer ($0 < y^+ < 30$–40) contains a significant amount of coherent structure and that repetitive processes can be identified that may control turbulence production and transport processes. However, laboratory measurements of the fluctuating

* Currently with Mobil Research and Development Corporation, Dallas Research Laboratory, 13777 Midway Road, Dallas, TX 75244, U.S.A.

0271–2091/91/180999–30$15.00

Received 6 July 1990
Revised 22 January 1991

velocity field have not provided enough information to link turbulence production and turbulent transport to turbulence structure. Furthermore, statistical correlations appearing in the transport equations for average quantities are unavailable since they involve pressure and spatial derivatives which are very difficult, if not impossible, to measure. The simulation of turbulent flow on a computer can provide, at each time step, the entire velocity, pressure and temperature fields simultaneously without interfering with the flow. All desired statistical quantities can be computed and time-dependent structural information is also made available.

Numerical calculations of turbulent flow usually employ models in order to simplify the transport equations. The simplest models calculate average velocity or average scalar fields by using closure models for the statistical properties of the turbulent fluctuations. The large-eddy simulation (LES) approach solves the full three-dimensional time-dependent equations with a coarse grid and models the effect of the subgrid-scale turbulence on the resolvable scales.[1-3] In the simple eddy or coherent structure modelling an attempt is made to model the organized quasi-periodic eddy structures in the viscous wall region of a bounded turbulent flow.[4-6] Direct numerical simulations (DNSs) which employ no simplification of the dynamic equations have only recently been performed for wall-bounded turbulent flows.[7-12]

The primary purpose of this study was to develop a direct numerical simulation of fully developed turbulent channel flow and passive heat transfer with the goal of studying wall eddy structure and its relationship to turbulence production and scalar transport. The two-dimensional channel was chosen because its geometric simplicity reduces the complexity of the numerical methods. In general, the dynamics of the turbulent flow field and the fluctuating temperature field are coupled. The thermal energy balance is coupled to the momentum balance through convection, and the momentum balance is coupled to the thermal energy balance through the temperature dependence of the fluid viscosity and density. However, for small temperature differences the influence of temperature on the physical properties of the fluid can be neglected and thus the momentum balance is decoupled from the thermal energy balance.

The first direct numerical simulation of channel flow was that of Orszag and Kells.[7] They performed a study of the non-linear stages of the transition from laminar to turbulent channel flow. Pseudospectral methods that use Fourier series expansions in the spanwise and streamwise directions and Chebyshev polynomial series expansions in the normal direction perpendicular to the walls were used. The algorithm made use of a time-splitting method that involves three fractional steps for the computation of the non-linear term, the pressure term and the viscous term in the Navier–Stokes equations. The splitting method introduced an error in that viscous effects are not included in the computation of the pressure and, as a consequence, the continuity equation was not satisfied at the wall. Orszag and Patera[8] simulated turbulent flow in a channel by using the Orszag and Kells algorithm with a fully explicit Adams–Bashforth scheme to time advance the non-linear terms. The resolution in their simulation was 64 grid points in both the streamwise and spanwise directions and 65 grid points in the direction normal to the channel walls. The results obtained were not for steady state turbulence. The initial condition for their flow was a random perturbation of Poiseuille flow and they integrated in time until the average wall shear stress reached a maximum so that the flow was approximately stationary. The results that were presented were taken from the flow fields near the time when the wall shear stress had reached a maximum.

The Orszag and Kells algorithm is satisfactory as long as it is used for high-Reynolds-number flows for which the behaviour at the wall is not critical. Marcus[9] developed a modification of the Orszag and Kells algorithm that incorporates viscous effects into the pressure and satisfies continuity at the walls. The Marcus modification involves the use of Green functions (capacitance

or influence matrix methods) to improve the implementation of the boundary conditions. It must be pointed out that, even with this modification, the flow field is slightly compressible at the end of each time step, since the operations used to carry out the evaluations of the pressure and viscous terms involve time-differencing errors; the error can be reduced with a smaller time step. Marcus used his algorithm to simulate Taylor–Couette flow (where for this problem the behaviour at the wall is critical to the entire flow field) and obtained excellent agreement with experimental measurements of wavy Taylor vortex flow.

Moser and Moin[10] developed a spectral method, following the lead of Leonard and Wray, [13] to simulate curved turbulent channel flow. The velocity field was represented using vector functions that inherently satisfied the continuity equation and the boundary conditions. Satisfying continuity removed one degree of freedom. The pressure was then eliminated from the equations to leave only two dependent variables to be solved. Their direct numerical simulation used $128 \times 65 \times 128$ spectral modes and their results are in excellent agreement with other experimental and theoretical results.

Kim *et al.*[12] simulated turbulent channel flow with a formulation, first discussed by Orszag and Patera,[8] that avoids time-splitting errors. Spectral methods using Fourier series expansions in the spanwise and streamwise directions and Chebyshev polynomial series expansions in the normal direction perpendicular to the walls were used. The Navier–Stokes equations were rewritten as a fourth-order equation for the normal component of the velocity and a second-order equation for the normal component of the vorticity. This was done by using the continuity equation and eliminating the pressure. This method is preferable to the time-splitting methods in that it satisfies continuity implicitly and requires less storage. The main disadvantage of this method is that it is considerably more complicated than the splitting methods; this may prove to be significant when other complications (e.g. non-Newtonian flow or wavy boundaries) are introduced. Their simulation was for a Reynolds number equal to 2800 (based on the bulk average velocity and half-channel height) and used $192 \times 129 \times 160$ spectral modes. Their results were shown to agree with available experimental results reported in the literature, except for the higher-order moments such as the skewness and flatness near the channel walls. They also reported that their results agree with results on a coarser mesh of $128 \times 129 \times 128$ and with the Moser and Moin[10] results obtained on a $128 \times 65 \times 128$ grid.

The technique used in the present study to solve the momentum balance is an adaptation of the Orszag–Kells approach to include the Marcus correction to the pressure. The velocity field is advanced in time with a fractional step approach that produces a velocity field that satisfies continuity exactly at both channel walls at the end of each time step. A similar approach to that of Circelli and McLaughlin[14] is used to solve the thermal energy balance. The results to be presented are for fully developed turbulent flow in a channel having a half-width H equal to 150 'wall' units (based on the kinematic viscosity and friction velocity) and a Prandtl number equal to one.[15] These results are compared with the velocity measurements of Niederschulte[16] and with temperature measurements reported in a series of articles by Corcoran, Page and co-workers.[17–19]

The value of this paper is that it fully documents how a pseudospectral code can be used to simulate turbulent flow in a channel, enabling readers to develop their own codes and simulations or to use existing codes with an understanding of how they work. Emphasis is placed on issues associated with the calculation of a fully developed turbulent field. Of interest are the studies of the influence of spatial and temporal resolution of the start-up procedure and of the time needed to reach a stationary state. The results are particularly important in evaluating turbulence studies, being done in several laboratories with this code, that are now appearing in the literature.

2. GOVERNING EQUATIONS

This time-dependent three-dimensional simulation predicts all three components of the velocity vector and the temperature as a function of time and all three spatial dimensions. The flow, which is driven by a constant mean pressure gradient, is for an incompressible Newtonian fluid of constant density, constant viscosity and constant thermal conductivity. The simulation assumes that body forces and viscous heating are negligible. The spatial vector (x, y, z) and the corresponding velocity vector (u, v, w) are shown in Figure 1 with the computational domain. The x-direction points downstream in the direction of the mean pressure gradient parallel to the walls, the y-direction points in the normal direction perpendicular to the walls and the z-direction points in the spanwise direction parallel to the walls. The computational domain is periodic in the streamwise and spanwise directions with corresponding periodicity lengths λ_x and λ_z. The distance between the channel walls is $2H$.

2.1. *Momentum transport*

The equation describing the model flow is the Navier–Stokes equation for an incompressible fluid with no body forces:

$$\frac{\partial \mathbf{v}}{\partial t} = -\mathbf{v}\cdot\nabla\mathbf{v} - \frac{1}{\rho}\nabla p + \frac{\mu}{\rho}\nabla^2\mathbf{v}, \tag{1}$$

$$\nabla\cdot\mathbf{v} = 0. \tag{2}$$

These equations are solved with a spectral method that expands the velocity field in terms of truncated Fourier series and Chebyshev polynomial series. The convective term when represented by truncated Fourier series violates conservation of energy, leading to unconditional instability of the equations.[20] In order to conserve energy, the convective term is rewritten using the following identity:

$$\mathbf{v}\cdot\nabla\mathbf{v} = -\mathbf{v}\times\boldsymbol{\omega} + \tfrac{1}{2}\nabla(\mathbf{v}\cdot\mathbf{v}), \tag{3}$$

where the vorticity vector is defined as

$$\boldsymbol{\omega} = \nabla\times\mathbf{v}. \tag{4}$$

The Navier–Stokes equation can then be written in the 'rotation' form

$$\frac{\partial \mathbf{v}}{\partial t} = \mathbf{v}\times\boldsymbol{\omega} - \nabla\pi + \nu\nabla^2\mathbf{v}, \tag{5}$$

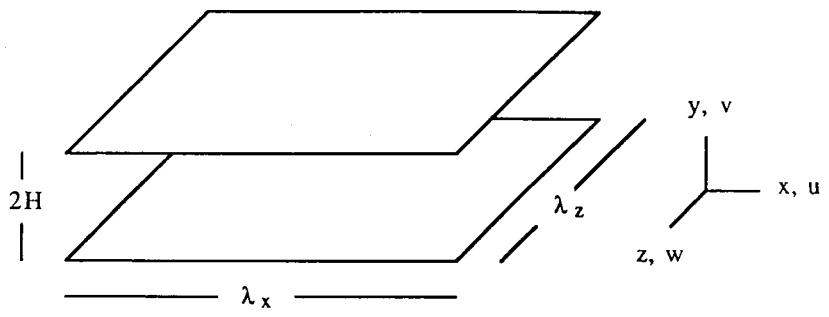

Figure 1. Computational domain

where π is the dynamic pressure head:

$$\pi=\frac{p}{\rho}+\tfrac{1}{2}\mathbf{v}\cdot\mathbf{v}. \tag{6}$$

The equation is made dimensionless using wall variables ν, the kinematic viscosity, and u_*, the friction velocity, where

$$u_*=\sqrt{\left(\frac{|\tau_w|}{\rho}\right)}, \qquad \tau_w=\mu\left.\frac{dU}{dy}\right|_{\text{wall}}. \tag{7}$$

The Navier–Stokes equation then becomes

$$\frac{\partial\mathbf{v}^+}{\partial t^+}=\mathbf{v}^+\times\boldsymbol{\omega}^+-\nabla^+\pi^+ +\nabla^{+2}\mathbf{v}^+, \tag{8}$$

$$\nabla^+\cdot\mathbf{v}^+=0. \tag{9}$$

By doing a force balance on the channel, one obtains the following relationship for constant mean pressure gradient:

$$-\frac{dP^+}{dx^+}=\frac{1}{H^+}. \tag{10}$$

Therefore (8) can be rewritten as

$$\frac{\partial\mathbf{v}^+}{\partial t^+}=\mathbf{v}^+\times\boldsymbol{\omega}^+-\nabla^+\pi^+ +\frac{1}{H^+}\mathbf{e}_x^+ +\nabla^{+2}\mathbf{v}^+, \tag{11}$$

with

$$\pi^+=p'^+ +\tfrac{1}{2}\mathbf{v}^+\cdot\mathbf{v}^+. \tag{12}$$

The term p' is the fluctuating component of the pressure. Equations (9) and (11) are the equations that are solved numerically.

These equations are subject to periodic boundary conditions in the streamwise and spanwise directions and the no-slip, no-penetration boundary condition is enforced at the channel walls:

$$\mathbf{v}^+(x^+ +\lambda_x^+, y^+, z^+ +\lambda_z^+, t^+)=\mathbf{v}^+(x^+, y^+, z^+, t^+), \tag{13}$$

$$\mathbf{v}^+(x^+, \pm H^+, z^+, t^+)=0. \tag{14}$$

The use of periodic boundary conditions is justified as long as λ_x and λ_z are large enough so that all two-point correlation functions become negligibly small at separation distances of $\lambda_x/2$ in the x-direction and $\lambda_z/2$ in the z-direction. This indicates that all important length scales have been resolved.

The initial condition for the hydrodynamics was a mean parabolic profile for laminar flow with random velocity fluctuations superimposed upon it. The streamwise and spanwise velocity fluctuations were specified by a random number generator and scaled to be of the order of one-hundredth of the mean velocity. The normal velocity fluctuations were then determined by satisfying continuity, (9).

2.2. Heat transport

The law of conservation of energy for an open, unsteady state system for a pure fluid of constant density and constant thermal conductivity flowing through a stationary volume is the

time-dependent three-dimensional advection–diffusion equation with a source term:

$$\frac{\partial T}{\partial t} = -\mathbf{v}\cdot\nabla T + \frac{k}{\rho C_p}\nabla^2 T + \frac{\mu}{\rho C_p}\Phi_v, \tag{15}$$

The temperature is transformed using $T=\theta - ay$, since this allows (15) to be solved with homogeneous boundary conditions for the problem to be studied:

$$\frac{\partial \theta}{\partial t} = -\mathbf{v}\cdot\nabla\theta + a\mathbf{v}\cdot\mathbf{e}_y + \frac{k}{\rho C_p}\nabla^2\theta + \frac{\mu}{\rho C_p}\Phi_v. \tag{16}$$

Equation (16) is made dimensionless using wall variables ν, u_* and t_*, the friction temperature, where

$$t_* = \frac{q_w}{\rho C_p u_*}, \qquad q_w = -k\left.\frac{dT}{dy}\right|_{wall}. \tag{17}$$

The energy balance equation then becomes

$$\frac{\partial \theta^+}{\partial t^+} = -\mathbf{v}^+\cdot\nabla^+\theta^+ + a^+\mathbf{v}^+\cdot\mathbf{e}_y^+ + \frac{1}{Pr}\nabla^{+2}\theta^+ + \frac{Br}{Pr}\Phi_v^+, \tag{18}$$

where the Prandtl number Pr and Brinkman number Br are defined as

$$Pr = \frac{\mu C_p}{k}, \qquad Br = \frac{\mu\rho C_p u_*^3}{k q_w}. \tag{19}$$

The heat production by viscous dissipation is assumed negligible compared to the heat transport by conduction. Thus the Brinkman number is set to zero:

$$\frac{\partial \theta^+}{\partial t^+} = -\mathbf{v}^+\cdot\nabla^+\theta^+ + a^+\mathbf{v}^+\cdot\mathbf{e}_y^+ + \frac{1}{Pr}\nabla^{+2}\theta^+. \tag{20}$$

Equation (20) is the model equation for heat transfer and is subject to periodic boundary conditions in the streamwise and spanwise directions and homogeneous boundary conditions at the channel walls:

$$\theta^+(x^+ + \lambda_x^+, y^+, z^+ + \lambda_z^+, t^+) = \theta^+(x^+, y^+, z^+, t^+), \tag{21}$$

$$\theta^+(x^+, \pm H^+, z^+, t^+) = 0. \tag{22}$$

All quantities will be presented in wall units so the superscript '+' will be dropped for convenience throughout the remainder of this paper.

The initial condition for the temperature profile was a mean conduction profile, $\theta = 0$ (or $T = -ay$). The heat transfer simulation was started after the hydrodynamic simulation had reached a stationary state, so it was not necessary to superimpose any temperature fluctuations on the mean profile. The turbulent velocity fluctuations quickly generated a turbulent temperature field.

3. NUMERICAL ALGORITHM

The velocity field is advanced in time from time step N to time step $N+1$ using three fractional steps. At each fractional step the velocity field is subject to periodic boundary conditions in the spanwise and streamwise directions, (13). The no-slip, no-penetration boundary condition (14) is enforced in the third fractional step.

The first fractional step accounts for the non-linear convective term and the mean pressure gradient. These terms are evaluated with second-order accuracy in Δt.

$$\frac{\partial \mathbf{v}^{N+1/3}}{\partial t} = \mathbf{v} \times \boldsymbol{\omega} + \frac{1}{H}\mathbf{e}_x. \tag{23}$$

In order to reduce convective instability, the largest contribution to the convective term is subtracted out and treated implicitly using a Crank–Nicholson scheme. This term is modelled as

$$\bar{U}^N(y)\frac{\partial \mathbf{v}}{\partial x}. \tag{24}$$

Thus (23) becomes

$$\frac{\partial \mathbf{v}^{N+1/3}}{\partial t} + \bar{U}^N(y)\frac{\partial \mathbf{v}}{\partial x} = \mathbf{v} \times \boldsymbol{\omega} + \frac{1}{H}\mathbf{e}_x + \bar{U}^N(y)\frac{\partial \mathbf{v}}{\partial x} = \mathbf{f} + \bar{U}^N(y)\frac{\partial \mathbf{v}}{\partial x}. \tag{25}$$

The right-hand side of (25) is treated explicitly using an Adams–Bashforth scheme. This semi-implicit Adams–Bashforth–Crank–Nicholson (ABCN) scheme is second-order-accurate in Δt.

$$\frac{\mathbf{v}^{N+1/3} - \mathbf{v}^N}{\Delta t} + \frac{\bar{U}^N(y)}{2}\left(\frac{\partial \mathbf{v}^{N+1/3}}{\partial x} + \frac{\partial \mathbf{v}^{N-2/3}}{\partial x}\right) = \frac{3}{2}\left(\mathbf{f}^N + \bar{U}^N(y)\frac{\partial \mathbf{v}^{N-2/3}}{\partial x}\right) - \frac{1}{2}\left(\mathbf{f}^{N-1} + \bar{U}^N(y)\frac{\partial \mathbf{v}^{N-5/3}}{\partial x}\right). \tag{26}$$

At the end of the first fractional step the streamwise velocity is non-zero at the wall because of the external pressure gradient and the fact that the step is inviscid. The other two intermediate velocity components are zero at the wall.

The second fractional step accounts for the inviscid contribution of the dynamic pressure head term. An implicit Euler scheme is used which is first-order-accurate in Δt.

$$\frac{\partial \mathbf{v}^{N+2/3}}{\partial t} = \frac{\partial \mathbf{v}^{N+1/3}}{\partial t} - \nabla \pi^{N+1}$$

or

$$\mathbf{v}^{N+2/3} = \mathbf{v}^{N+1/3} - \Delta t \nabla \pi^{N+1}. \tag{27}$$

The pressure head term is evaluated by requiring that the velocity field after the second fractional step be divergence-free ('projection step'[21]). Taking the divergence of (27), we get upon rearrangement

$$\nabla^2 \pi^{N+1} = \frac{\nabla \cdot \mathbf{v}^{N+1/3}}{\Delta t}, \tag{28}$$

subject to

$$\frac{\partial \pi^{N+1}}{\partial y}(x, \pm H, z, t) = \frac{\partial^2 \mathbf{v}^{N+1}}{\partial y^2}(x, \pm H, z, t) \cdot \mathbf{e}_y. \tag{29}$$

The pressure equation is a linear inhomogeneous equation with inhomogeneous boundary conditions. Thus the solution can be divided into two parts: the first part satisfies the inhomogeneous equation with homogeneous boundary conditions and the second part satisfies the homogeneous equation with inhomogeneous boundary conditions. The pressure head term is decomposed into the inviscid part π_i and the viscous part π_v:

$$\pi = \pi_i + \pi_v. \tag{30}$$

The inviscid part of the pressure head satisfies the inhomogeneous equation with homogeneous boundary conditions and is solved for the second fractional step:

$$\nabla^2 \pi_i^{N+1} = \frac{\nabla \cdot \mathbf{v}^{N+1/3}}{\Delta t}, \tag{31}$$

$$\frac{\partial \pi_i^{N+1}}{\partial y}(x, \pm H, z, t) = 0. \tag{32}$$

At the end of the second fractional step, both the streamwise and spanwise components of the velocity are non-zero on the walls, once again because the effects of viscosity have not been included. The normal velocity component does vanish on the wall.

The third fractional step accounts for viscous effects. The viscous part of the pressure head satisfies the homogeneous equation with inhomogeneous boundary conditions:

$$\nabla^2 \pi_v^{N+1} = 0, \tag{33}$$

$$\frac{\partial \pi_v^{N+1}}{\partial y}(x, \pm H, z, t) = \frac{\partial^2 \mathbf{v}^{N+1}}{\partial y^2}(x, \pm H, z, t) \cdot \mathbf{e}_y. \tag{34}$$

Equation (34) is satisfied if and only if[22]

$$\nabla \cdot \mathbf{v}^{N+1}(x, \pm H, z, t) = 0. \tag{35}$$

Thus continuity is satisfied at the walls.

An implicit backward Euler scheme is used for the viscous term which is first-order-accurate in Δt. Marcus[9] tried a Crank–Nicholson scheme for the viscous term in his work but claimed it produced spurious oscillations.

$$\frac{\partial \mathbf{v}^{N+1}}{\partial t} = \frac{\partial \mathbf{v}^{N+2/3}}{\partial t} + \nabla^2 \mathbf{v}^{N+1}$$

or

$$(1 - \Delta t \nabla^2)\mathbf{v}^{N+1} = \mathbf{v}^{N+2/3}. \tag{36}$$

Equation (36) is solved subject to

$$\mathbf{v}^{N+1}(x, \pm H, z, t) = 0. \tag{37}$$

Note that the velocity at time step $N+1$ appears in the boundary conditions, (34). Therefore (33), (34), (36) and (37) have to be solved simultaneously and for this purpose π_v is expanded in a set of Green's functions.

Owing to the explicit treatment of the non-linear convective term, there is a CFL stability constraint on the size of the time step Δt:

$$1 > \Delta t \left(\left| \frac{u(x, y, z, t)}{\Delta x} \right| + \left| \frac{v(x, y, z, t)}{\Delta y(y)} \right| + \left| \frac{w(x, y, z, t)}{\Delta z} \right| \right). \tag{38}$$

This condition was determined by computing the term on the right-hand side of (38) while varying Δt. We found that the integration quickly diverged once this quantity reached unity anywhere in the flow field. By decreasing Δt so that this term was kept less than unity, a stable integration was obtained.

The heat transport equation is advanced in time from N to $N+1$ using two fractional steps. At each fractional step the solution is subject to periodic boundary conditions in the spanwise and

streamwise directions, (21). The first fractional step accounts for the convective term. As for the time advancement of the velocity field, (26), and ABCN scheme is used in order to reduce convective instability.

$$\frac{\partial\theta^{N+1/3}}{\partial t}=-\mathbf{v}\cdot\nabla\theta+a\mathbf{v}\cdot\mathbf{e}_y,$$

$$\frac{\partial\theta^{N+1/3}}{\partial t}+\bar{U}^N(y)\frac{\partial\theta}{\partial x}=-\mathbf{v}\cdot\nabla\theta+a\mathbf{v}\cdot\mathbf{e}_y+\bar{U}^N(y)\frac{\partial\theta}{\partial x}=g+\bar{U}^N(y)\frac{\partial\theta}{\partial x},$$

$$\frac{\theta^{N+1/3}-\theta^N}{\Delta t}+\frac{\bar{U}^N(y)}{2}\left(\frac{\partial\theta^{N+1/3}}{\partial x}+\frac{\partial\theta^{N-2/3}}{\partial x}\right)=\frac{3}{2}\left(g^N+\bar{U}^N(y)\frac{\partial\theta^{N-2/3}}{\partial x}\right)$$
$$-\frac{1}{2}\left(g^{N-1}+\bar{U}^N(y)\frac{\partial\theta^{N-5/3}}{\partial x}\right). \tag{39}$$

The second fractional step accounts for the diffusion term. An implicit backward Euler scheme is used.

$$\frac{\partial\theta^{N+1}}{\partial t}=\frac{\partial\theta^{N+1/3}}{\partial t}+\frac{1}{Pr}\nabla^2\theta^{N+1}$$

or

$$\left(1-\frac{\Delta t}{Pr}\nabla^2\right)\theta^{N+1}=\theta^{N+1/3}. \tag{40}$$

Equation (40) is subject to

$$\theta^{N+1}(x,\pm H,z,t)=0. \tag{41}$$

Note the similarity of (36) and (37) to (40) and (41). The same solution procedure is used for both sets of equations.

4. SPECTRAL REPRESENTATION

The transport equations (11) and (20) are subject to periodic boundary conditions in the streamwise and spanwise directions. Because periodic boundary conditions are used in the x- and z-directions, the velocity, pressure head and temperature fields are expanded in terms of Fourier series in these directions. In order to obtain adequate resolution in the normal direction at the wall and to satisfy the rigid boundary conditions there, the y-variation of the velocity, pressure head and temperature fields is expanded in terms of Chebyshev polynomial series. Chebyshev polynomial expansions have rapid convergence properties at the boundaries and, unlike Fourier series expansions, do not exhibit the Gibbs phenomenon at the boundaries.[23].

$$\mathbf{v}(x,y,z,t)=\sum_{l=-N_x/2}^{N_x/2-1}\sum_{m=-N_z/2}^{N_z/2-1}\sum_{n=0}^{N_y}\tilde{\mathbf{v}}(l,n,m,t)\exp\left[2\pi i\left(\frac{lx}{\lambda_x}+\frac{mz}{\lambda_z}\right)\right]T_n\left(\frac{y}{H}\right). \tag{42}$$

The nth-order Chebyshev polynomial is defined as

$$T_n\left(\frac{y}{H}\right)=\cos(n\theta),\quad\text{where }\theta=\cos^{-1}\left(\frac{y}{H}\right). \tag{43}$$

The pressure head and temperature fields are similarly expanded. The representation of the fields

as $\mathbf{v}(x, y, z, t)$ is termed 'physical space' and the representation as $\tilde{\mathbf{v}}(l, n, m, t)$ is termed 'spectral space'.

A discrete set of grid points is introduced with

$$x_h = \frac{h\lambda_x}{N_x}, \qquad h = 0, 1, \ldots, N_x - 1$$

$$z_j = \frac{j\lambda_z}{N_z}, \qquad j = 0, 1, \ldots, N_z - 1,$$

$$y_k = H\cos\left(\frac{k\pi}{N_y}\right), \quad k = 0, 1, \ldots, N_y. \tag{44}$$

Using (44), equation (42) can be rewritten as

$$\mathbf{v}(x_h, y_k, z_j, t) = \sum_{l=0}^{N_x-1} \sum_{m=0}^{N_z-1} \sum_{n=0}^{N_y} \tilde{\mathbf{v}}(l, n, m, t) \exp\left[2\pi i\left(\frac{hl}{N_x} + \frac{jm}{N_z}\right)\right] T_n\left(\frac{y_k}{H}\right). \tag{45}$$

Note that the Chebyshev polynomial series can also be written as a Fourier series:

$$\mathbf{v}(x_h, y_k, z_j, t) = \sum_{l=0}^{N_x-1} \sum_{m=0}^{N_z-1} \sum_{n=0}^{2N_y-1} \tilde{\mathbf{u}}(l, n, m, t) \exp\left[2\pi i\left(\frac{hl}{N_x} + \frac{jm}{N_z} + \frac{kn}{2N_y}\right)\right], \tag{46}$$

with

$$\tilde{\mathbf{u}}(l, 0, m, t) = \tilde{\mathbf{v}}(l, 0, m, t), \qquad \tilde{\mathbf{u}}(l, N_y, m, t) = \tilde{\mathbf{v}}(l, N_y, m, t)$$

and, for $n \neq 0$ and $n \neq N_y$,

$$\tilde{\mathbf{u}}(l, n, m, t) = \tilde{\mathbf{u}}(l, -n, m, t) = \tfrac{1}{2}\tilde{\mathbf{v}}(l, n, m, t).$$

The coefficients of the series expansions are determined by forcing the series to be an exact representation of the corresponding field at the grid points and are computed from

$$\tilde{\mathbf{v}}(l, n, m, t) = \frac{1}{2N_x N_z N_y} \sum_{h=0}^{N_x-1} \sum_{j=0}^{N_z-1} \sum_{k=0}^{2N_y-1} \mathbf{v}(x_h, y_k, z_j, t) \exp\left[-2\pi i\left(\frac{hl}{N_x} + \frac{jm}{N_z} + \frac{kn}{2N_y}\right)\right]. \tag{47}$$

Since the velocity, pressure head and temperature fields are real functions, the corresponding coefficients of their series expansions are complex conjugate symmetric. Therefore only half of the spectral coefficients need to be computed and stored.[24] The summations required in (46) and (47) are performed by fast Fourier transform (FFT).

The computation of the product of two functions represented by truncated Fourier series produces aliasing errors, whereby the energy of smaller wavelengths is misrepresented because large wave numbers are generated and these wave numbers are not orthogonal to the basis functions on the grid used in the calculations. The result is that the energies of the top half of the wave number spectrum contain spurious contributions. Aliasing errors are reduced by use of the 'two-thirds' rule in the x- and z-directions.[25] The top one-third of the wave numbers are zeroed and then the functions are transformed to physical space where the multiplication is carried out. Then the product is transformed back into spectral space. This occurs in the convective fractional step when the cross product of the vorticity and velocity fields is computed and when the dot product of the velocity field and the gradient of the temperature field is computed.

Interpolation from low grid resolutions to higher grid resolutions was done in spectral space. To interpolate from an $N_x \times N_z \times (N_y+1)$ grid to a $N'_x \times N'_z \times (N'_y+1)$ grid, where $N_x < N'_x$, $N_z < N'_z$ and $N_y < N'_y$, the following was used:

$$\tilde{\mathbf{v}}'(l,n,m) = \begin{cases} \tilde{\mathbf{v}}(l,n,m), & \text{where } 1 \leqslant N_x,\ n \leqslant N_y,\ m \leqslant N_z, \\ 0, & \text{otherwise.} \end{cases} \tag{48}$$

5. SOLUTION PROCEDURE

The spectral representations of the velocity, pressure head and temperature fields are substituted into the finite difference equations, reducing the problem from solving partial differential equations for the physical fields to solving ordinary differential equations for the spectral coefficients of the physical fields.

5.1. Convective fractional step

The term **f** in (26) is computed in physical space:

$$f_x = v\omega_z - w\omega_y + \frac{1}{H}, \qquad f_y = w\omega_x - u\omega_z, \qquad f_z = u\omega_y - v\omega_x. \tag{49}$$

The vorticity field is first computed in spectral space. Then the vorticity and velocity fields are transformed to physical space using the FFT (46), and (49) is computed at the grid points (x_h, y_k, z_j). The **f**-field is transformed to spectral space using the FFT (47).

The term g in (39) is similarly computed in physical space:

$$g = -u\frac{\partial \theta}{\partial x} - v\frac{\partial \theta}{\partial y} - w\frac{\partial \theta}{\partial z} + av. \tag{50}$$

The gradient of the θ-field is computed in spectral space and transformed to physical space, where (50) is computed at the grid points. The g-field is then transformed to spectral space.

The spectral expansions for the velocity and temperature fields are substituted into equations (26) and (39) and upon rearrangement one obtains

$$\tilde{\mathbf{v}}^{N+1/3} = \frac{\tilde{\mathbf{v}}^N + \Delta t(\tfrac{3}{2}\tilde{\mathbf{f}}^N - \tfrac{1}{2}\tilde{\mathbf{f}}^{N-1}) + \Delta t(\pi i l \bar{U}^N(n)/\lambda_x)(2\tilde{\mathbf{v}}^{N-2/3} - \tilde{\mathbf{v}}^{N-5/3})}{1 + \Delta t(\pi i l \bar{U}^N(n)/\lambda_x)}, \tag{51}$$

$$\tilde{\theta}^{N+1/3} = \frac{\tilde{\theta}^N + \Delta t(\tfrac{3}{2}\tilde{g}^N - \tfrac{1}{2}\tilde{g}^{N-1}) + \Delta t(\pi i l \bar{U}^N(n)/\lambda_x)(2\tilde{\theta}^{N-2/3} - \tilde{\theta}^{N-5/3})}{1 + \Delta t(\pi i l \bar{U}^N(n)/\lambda_x)}. \tag{52}$$

Equations (51) and (52) are solved explicitly for the velocity and temperature fields in spectral space (l, n, m) after the first (convective) fractional time step. (It is understood that all spectral fields are functions of (l, n, m) unless otherwise noted.) A total of 13 FFTs are computed in this fractional step using 55% of the CPU time (using Cray SCILIB routines CFFT2, CRFFT2 and RCFFT2).

5.2. Pressure fractional step

The spectral expansions for the velocity and inviscid pressure head fields are substituted into (31):

$$-4\pi^2\left(\frac{l^2}{\lambda_x^2}+\frac{m^2}{\lambda_z^2}\right)\tilde{\pi}_i^{N+1}(l,n,m)+\frac{1}{H^2c_n}\sum_{\substack{p=n+2\\ p+n\text{ even}}}^{N_y}p(p^2-n^2)\tilde{\pi}_i^{N+1}(l,p,m)$$

$$=\frac{2\pi i}{\Delta t}\left(\frac{l}{\lambda_x}+\frac{m}{\lambda_z}\right)\tilde{v}^{N+1/3}(l,n,m)+\frac{2}{Hc_n}\sum_{\substack{p=n+1\\ p+n\text{ odd}}}^{N_y}p\tilde{v}^{N+1/3}(l,p,m),\quad 2\leqslant n\leqslant N_y, \tag{53}$$

where $c_0=2$ and $c_n=1$ $(n>0)$. The right-hand side of (53) can be computed directly. For notational convenience the (l, m) dependence will be dropped and the right-hand side of (53) will be denoted by $f(n)/H^2$. Equation (53) can then be rewritten as

$$\sum_{\substack{p=n+2\\ p+n\text{ even}}}^{N_y}p^3\tilde{\pi}_i^{N+1}(p)-n^2\sum_{\substack{p=n+2\\ p+n\text{ even}}}^{N_y}p\tilde{\pi}_i^{N+1}(p)-kc_n\tilde{\pi}_i^{N+1}(n)=c_nf(n),\quad 2\leqslant n\leqslant N_y, \tag{54}$$

where

$$k=4\pi^2H^2\left(\frac{l^2}{\lambda_x^2}+\frac{m^2}{\lambda_z^2}\right).$$

This linear system of equations can be converted into a nearly tridiagonal system of equations that are essentially diagonally dominant and are thus not ill-conditioned for inversion[23] (note that there is a sign error in equation (10.10) of the 1st edition of Reference 23):

$$\frac{kc_{n-2}}{4n(n-1)}\tilde{\pi}_i^{N+1}(n-2)-\left(1+\frac{ke_{n+2}}{2(n^2-1)}\right)\tilde{\pi}_i^{N+1}(n)+\frac{ke_{n+4}}{4n(n+1)}\tilde{\pi}_i^{N+1}(n+2)$$

$$=-\frac{c_{n-2}f(n-2)}{4n(n-1)}+\frac{e_{n+2}f(n)}{2(n^2-1)}-\frac{e_{n+4}f(n+2)}{4n(n+1)},\quad 2\leqslant n\leqslant N_y, \tag{55}$$

where

$$e_n=1\quad\text{for } n\leqslant N_y,\qquad e_n=0\quad\text{for } n>N_y.$$

Equation (55) is a system of N_y-2 equations involving N_y unknowns. Note that the even Chebyshev polynomial coefficients depend only on even Chebyshev polynomial coefficients and the odd Chebyshev polynomial coefficients depend only on odd Chebyshev polynomial coefficients. The other two equations required to solve the system (55) come from applying the Neumann boundary conditions (32). Expanding π_i in a Chebyshev polynomial series and substituting into (32), one obtains upon some rearrangement a condition on the odd $\pi_i(n)$,

$$\sum_{\substack{p=1\\ p\text{ odd}}}^{N_y-1}p^2\tilde{\pi}_i(p)=0, \tag{56}$$

and a condition on the even $\pi_i(n)$,

$$\sum_{\substack{p=2\\ p\text{ even}}}^{N_y}p^2\tilde{\pi}_i(p)=0. \tag{57}$$

Equations (55)–(57) are solved for the $\pi_i(n)$. Since the odd Chebyshev polynomial coefficients depend only on odd Chebyshev polynomial coefficients and the even Chebyshev polynomial coefficients depend only on even Chebyshev polynomial coefficients, these equations can be reduced to solving two systems of equations, one system for the $N_y/2+1$ even Chebyshev polynomial coefficients and the second system for the $N_y/2$ odd Chebyshev polynomial coefficients. Each linear system can be written in block matrix form:

$$\begin{bmatrix} \mathbf{A} & \mathbf{B} \\ \mathbf{C} & D \end{bmatrix} \begin{bmatrix} x(1) \\ x(2) \\ — \\ — \\ — \\ — \\ x(N-1) \\ x(N) \end{bmatrix} = \begin{bmatrix} y(1) \\ y(2) \\ — \\ — \\ — \\ — \\ y(N-1) \\ y(N) \end{bmatrix}, \tag{58}$$

where **A** is a tridiagonal matrix, **B** is a column vector, **C** is a row vector and D is a scalar. This matrix is inverted by **LU** decomposition. Equation (58) is inverted for each (l, m) wave number for a total of $N_xN_z/2$ inversions of an $(N_y/2)\times(N_y/2)$ matrix and $N_xN_z/2$ inversions of an $(N_y/2+1)\times(N_y/2+1)$ matrix.

M is factored into **LU**:

$$\begin{bmatrix} \mathbf{l} & 0 \\ \mathbf{q} & 1 \end{bmatrix} \begin{bmatrix} \mathbf{u} & \mathbf{p} \\ 0 & d \end{bmatrix} = \begin{bmatrix} \mathbf{A} & \mathbf{B} \\ \mathbf{C} & D \end{bmatrix},$$

where **l** and **u** are the **lu** decomposition of **A**, **q** is a row vector where $\mathbf{qu}=\mathbf{C}$, **p** is a column vector where $\mathbf{lp}=\mathbf{B}$, and d is a scalar where $\mathbf{qp}+d=D$. The **LU** decomposition is set up in the following order. First, the **lu** decomposition of the tridiagonal matrix **A** is performed:

$$\mathbf{l} = \begin{bmatrix} 1 & 0 & — & — \\ l(2) & 1 & 0 & — \\ 0 & l(3) & 1 & — \\ — & 0 & l(4) & — \\ — & — & 0 & — \\ — & — & — & — \\ — & — & — & — \end{bmatrix}, \qquad \mathbf{u} = \begin{bmatrix} d(1) & u(1) & 0 & — \\ 0 & d(2) & u(2) & — \\ — & 0 & d(3) & — \\ — & — & 0 & — \\ — & — & — & — \\ — & — & — & — \\ — & — & — & — \end{bmatrix}.$$

The first elements of d and u are solved by inspection and the rest of the elements of d, u and l are solved by recursion. Secondly, the row vector **q** is solved directly by forward substitution since **u** is an upper triangular matrix. Thirdly, the column vector **p** is solved directly by forward substitution since **l** is a lower triangular matrix. Fourthly, the scalar d is solved directly. Once the **LU** decomposition is set up, the solution of the unknown vector **x** is obtained by defining an intermediate vector **z** where $\mathbf{Ux}=\mathbf{z}$ and obtaining its solution by forward substitution $\mathbf{Lz}=\mathbf{y}$.

Then the unknown vector $\mathbf{x}$ is obtained by backward substitution $\mathbf{Ux}=\mathbf{z}$. The total floating point operations required for setting up the $\mathbf{LU}$ decomposition and solving for $\mathbf{x}$ is $19N-30$ for $\mathbf{M}$ defined to be $N\times N$. From our experience the inversion is not ill-conditioned.

Substituting (30) into (27) and defining

$$\mathbf{v}^{N+2/3}=\mathbf{v}_{\mathrm{i}}^{N+2/3}+\mathbf{v}_{\mathrm{v}}^{N+2/3}, \tag{59}$$

we obtain

$$\mathbf{v}_{\mathrm{i}}^{N+2/3}=\mathbf{v}^{N+1/3}-\Delta t\nabla\pi_{\mathrm{i}}^{N+1}, \tag{60}$$

$$\mathbf{v}_{\mathrm{v}}^{N+2/3}=-\Delta t\nabla\pi_{\mathrm{v}}^{N+1}. \tag{61}$$

The spectral expansions (42) are substituted into (60):

$$\tilde{u}_{\mathrm{i}}^{N+2/3}(l,n,m)=\tilde{u}^{N+1/3}(l,n,m)-\Delta t\left(\frac{2\pi il}{\lambda_x}\right)\tilde{\pi}_{\mathrm{i}}^{N+1}(l,n,m),$$

$$\tilde{v}_{\mathrm{i}}^{N+2/3}(l,n,m)=\tilde{v}^{N+1/3}(l,n,m)-\frac{2\Delta t}{Hc_n}\sum_{\substack{p=n+1\\ p+n\,\mathrm{odd}}}^{N_y}p\tilde{\pi}_{\mathrm{i}}^{N+1}(l,p,m),$$

$$\tilde{w}_{\mathrm{i}}^{N+2/3}(l,n,m)=\tilde{w}^{N+1/3}(l,n,m)-\Delta t\left(\frac{2\pi im}{\lambda_z}\right)\tilde{\pi}_{\mathrm{i}}^{N+1}(l,n,m). \tag{62}$$

Equations (62) are solved directly for the inviscid part of the velocity field after the second (pressure) fractional step.

The viscous pressure head must be computed from (33) and (34) before solving (59) for the velocity field after the second (pressure) fractional step. Expressing π_{v} as a spectral expansion, $\pi_{\mathrm{v}}(l,n,m)$ can be written as a linear combination of two linearly independent solutions of Laplace's equation (33):

$$\tilde{\pi}_{\mathrm{v}}^{N+1}(l,n,m)=a_1^{N+1}(l,m)\chi_1(l,n,m)+a_2^{N+1}(l,m)\chi_2(l,n,m). \tag{63}$$

The Laplace solutions χ_1 and χ_2 are calculated subject to arbitrary boundary conditions picked to ensure their linear independence:

$$\chi_1=1,\quad \chi_2=0\quad \text{at } y=-H, \tag{64}$$

$$\chi_1=0,\quad \chi_2=1\quad \text{at } y=H. \tag{65}$$

The Laplace solutions do not depend on the time step and are computed once. The Fourier modes $a_1(l,m)$ and $a_2(l,m)$ are solved by applying the boundary conditions (34). Using (59), equation (36) becomes

$$\mathbf{v}^{N+1}=(1-\Delta t\nabla^2)^{-1}\mathbf{v}_{\mathrm{i}}^{N+2/3}+(1-\Delta t\nabla^2)^{-1}\mathbf{v}_{\mathrm{v}}^{N+2/3}. \tag{66}$$

From the condition (35),

$$0=\nabla\cdot(1-\Delta t\nabla^2)^{-1}\mathbf{v}_{\mathrm{i}}^{N+2/3}+\nabla\cdot(1-\Delta t\nabla^2)^{-1}\mathbf{v}_{\mathrm{v}}^{N+2/3},\quad y=\pm H. \tag{67}$$

Substituting (61) and rearranging,

$$\Delta t\nabla\cdot(1-\Delta t\nabla^2)^{-1}\nabla\pi_{\mathrm{v}}^{N+1}=\nabla\cdot(1-\Delta t\nabla^2)^{-1}\mathbf{v}_{\mathrm{i}}^{N+2/3},\quad y=\pm H. \tag{68}$$

Substituting the spectral expansion (63), equation (68) becomes

$$\Delta t\nabla\cdot(1-\Delta t\nabla^2)^{-1}\nabla[a_1(l,m)\chi_1(l,n,m)+a_2(l,m)\chi_2(l,n,m)]=\nabla\cdot(1-\Delta t\nabla^2)^{-1}\mathbf{v}_{\mathrm{i}}^{N+2/3},\quad y=\pm H. \tag{69}$$

Note that this is two equations in two unknowns, a_1 and a_2, for each (l, m) wave number and can be written as

$$\begin{bmatrix} b_{11} & b_{12} \\ b_{21} & b_{22} \end{bmatrix} \begin{bmatrix} a_1 \\ a_2 \end{bmatrix} = \begin{bmatrix} d_1 \\ d_2 \end{bmatrix} \quad \text{for each } (l, m), \tag{70}$$

where

$$\begin{aligned} b_{11}(l, m) &= \Delta t \nabla \cdot (1 - \Delta t \nabla^2)^{-1} \nabla \chi_1(l, n, m) \quad \text{at } y = -H, \\ b_{12}(l, m) &= \Delta t \nabla \cdot (1 - \Delta t \nabla^2)^{-1} \nabla \chi_2(l, n, m) \quad \text{at } y = -H, \\ b_{21}(l, m) &= \Delta t \nabla \cdot (1 - \Delta t \nabla^2)^{-1} \nabla \chi_1(l, n, m) \quad \text{at } y = H, \\ b_{22}(l, m) &= \Delta t \nabla \cdot (1 - \Delta t \nabla^2)^{-1} \nabla \chi_2(l, n, m) \quad \text{at } y = H, \\ d_1(l, m) &= \nabla \cdot (1 - \Delta t \nabla^2)^{-1} \mathbf{v}_i^{N+2/3}(l, n, m) \quad \text{at } y = -H, \\ d_2(l, m) &= \nabla \cdot (1 - \Delta t \nabla^2)^{-1} \mathbf{v}_i^{N+2/3}(l, n, m) \quad \text{at } y = H. \end{aligned}$$

Equation (70) is trivial to solve. Note that the $b(l, m)$ coefficients are computed only once and the $d(l, m)$ coefficients are computed every time step. Once the Fourier modes $a_1(l, m)$ and $a_2(l, m)$, are computed, (63) is solved directly for the viscous pressure head. Then (59) is solved for the velocity field after the second (pressure) fractional step:

$$\begin{aligned} \tilde{u}^{N+2/3}(l, n, m) &= \tilde{u}_i^{N+2/3}(l, n, m) - \Delta t \left(\frac{2\pi i l}{\lambda_x} \right) \tilde{\pi}_v^{N+1}(l, n, m), \\ \tilde{v}^{N+2/3}(l, n, m) &= \tilde{v}_i^{N+2/3}(l, n, m) - \frac{2\Delta t}{H c_n} \sum_{p=n+1}^{N_y} p \tilde{\pi}_v^{N+1}(l, p, m), \\ \tilde{w}^{N+2/3}(l, n, m) &= \tilde{w}_i^{N+2/3}(l, n, m) - \Delta t \left(\frac{2\pi i m}{\lambda_z} \right) \tilde{\pi}_v^{N+1}(l, n, m). \end{aligned} \tag{71}$$

5.3. *Viscous diffusion fractional step*

The same solution procedure used for solving equations (31) and (32) is used to solve equations (36), (37), (40) and (41). The form of these equations is

$$(1 - \Delta t \nabla^2) r(x, y, z) = f(x, y, z), \tag{72}$$

$$r(x, \pm H, z) = 0, \tag{73}$$

$$r(x + \lambda_x, y, z + \lambda_z) = r(x, y, z). \tag{74}$$

The spectral representation (42) automatically satisfies (74). Upon substitution of (42) into (72) and (73),

$$\left[1 + 4\pi^2 \Delta t \left(\frac{l^2}{\lambda_x^2} + \frac{m^2}{\lambda_z^2} \right) \right] \tilde{r}(l, n, m) - \frac{\Delta t}{H^2} \sum_{\substack{p=n+2 \\ p+n \text{ even}}}^{N_y} p(p^2 - n^2) \tilde{r}(l, p, m) = \tilde{f}(l, n, m), \quad 2 \leqslant n \leqslant N_y, \tag{75}$$

$$\sum_{n=0}^{N_y} \tilde{r}(l, n, m) = 0, \tag{76}$$

$$\sum_{n=0}^{N_y} (-1)^n \tilde{r}(l, n, m) = 0. \tag{77}$$

Equation (75) is rewritten (dropping the (l, m) dependence for notational convenience) as

$$\sum_{p=n+2}^{N_y} p^3\tilde{r}(p)-n^2\sum_{p=n+2}^{N_y} p\tilde{r}(p)-kc_n\tilde{r}(n)=-\left(\frac{H^2}{\Delta t}\right)\tilde{f}(n), \quad 2\leqslant n\leqslant N_y, \tag{78}$$

where

$$k=\frac{H^2}{\Delta t}\left[1+4\pi^2\Delta t\left(\frac{l^2}{\lambda_x^2}+\frac{m^2}{\lambda_z^2}\right)\right].$$

This is the exact form of (54) and can be similarly converted into a nearly tridiagonal system of equations, (55).

The boundary conditions (76) and (77) can be subtracted to give a condition for the odd $r(n)$,

$$\sum_{\substack{n=1\\ n\,\text{odd}}}^{N_y-1}\tilde{r}(n)=0, \tag{79}$$

and added to give a condition for the even $r(n)$,

$$\sum_{\substack{n=0\\ n\,\text{even}}}^{N_y}\tilde{r}(n)=0. \tag{80}$$

As in Section 5.2, equations (78)–(80) can be written in the block matrix form (58) and are solved by the same procedure for u, v, w and θ at time step $N+1$.

6. TURBULENT CHANNEL FLOW WITH HEAT TRANSFER

The main input parameters for the simulation are the computational box lengths and the Prandtl number. The half-channel height fixes the Reynolds number for the hydrodynamics (equation (10)). The computational domain for the simulations was $H=150$, $\lambda_x=1900$ and $\lambda_z=950$. The Prandtl number was fixed at 1·0 and the coefficient a defined in (16) was also 1·0. The only parameters that changed during the course of the simulation were the number of grid points and the size of the time step (Tables I and II). The heat transfer calculation was not added until after the hydrodynamic simulation had progressed in time 12 500 wall units. The time step was kept as large as possible throughout each run in order to reach a stationary state quickly without violating the Courant condition (38). Once a stationary state was reached, the time step was dropped to between 0·2 and 0·25 to compute statistics. Statistical averages are only functions of the normal direction, so averages were taken over the x- and z-directions and in time. It was determined that the time step had little effect on the computed statistics.

Table I. Computational grids

	Physical grid			Spectral mode			Effective grid spacing		
Run	N_x	N_y	N_z	N_x	N_y	N_z	Δx	Δy	Δz
A	16	33	64	10	33	42	190·0	0·72–14·7	22·6
B	32	65	128	21	65	85	90·5	0·18–7.4	11·2
C	64	65	128	42	65	85	45·2	0·18–7·4	11·2
D	128	65	128	85	65	85	22·4	0·18–7·4	11·2

Table II. Simulation run times

Run	Time step		Δt	Total simulation time
	Start	Finish		
A	0	80000	0·005	400
	80000	250000	0·01	2100
	250000	270000	0·05	3100
	270000	300000	0·08	5500
	300000	340000	0·1	9500
	340000	440000	0·05	14500
	440000	460000	0·2	18500
	460000	580000	0·3	54500
	580000	583000	0·2	55100
B	581000	585000	0·2	55500
	585000	586000	0·5	56000
	586000	621000	0·4	70000
C	621000	630000	0·4	73600
	630000	630800	0·25	73800
D	630000	648500	0·25	78225

The initial condition for the flow field consisted of a mean parabolic profile for laminar flow with random velocity fluctuations superimposed upon it. The kinetic energy from the mean profile quickly transferred to the fluctuating velocity field, generating very large turbulent fluctuations. The time step during this period of the simulation had to be kept very small (0·005) in order to stabilize the integration. The mean velocity and turbulence intensities required an integration time of 12 500 (400 000 time steps) to reach a stationary state on the initial grid of 33 792 points. Another 183 000 time steps were integrated for a time of 42 600 in order to stabilize the higher-order statistics and to ensure a fully developed velocity and temperature field before interpolating up to more refined grids. The heat transfer calculation was started after the velocity field had been integrated for 400 000 time steps. The initial condition was a mean conduction profile ($T=-y$) with no fluctuations superimposed upon it. The turbulent velocity field quickly generated a turbulent temperature field.

Three interpolations were performed during the course of this simulation. The wall shear stress would adjust for each new grid. At first it would drop to between 0·85 and 0·9, then rise slowly to oscillate around the steady state value of 1·0. The time required for this adjustment varied for each interpolation. The wall shear stress for grid B adjusted within an integration time of 300. The adjustment required an integration time of 1400 for grid C and 3500 for grid D. The steady state Reynolds numbers (based on the half-channel height and either the centreline or bulk velocity) for each run are presented in Table III along with the centreline and bulk velocities. The wall heat flux also adjusted to a new steady state value on each grid. This is also presented in Table III along with the Nusselt number

$$Nu=\frac{hD_H}{k}=\frac{q_w 4H}{(T_w-T_c)k}. \tag{81}$$

The steady state velocity statistics obtained on the four grids are presented in Figures 2–11. Note that the legend for the physical grids presented on all the figures gives the resolution as

Table III. Bulk average quantities

Run	U_c	U_b	Re_c	Re_b	q_w	Nu
A	16·05	13·83	2407	2075	7·518	30·07
B	16·04	13·84	2405	2076	7·729	30·92
C	17·39	14·71	2609	2206	6·805	27·22
D	17·85	15·08	2678	2262	6·341	25·36

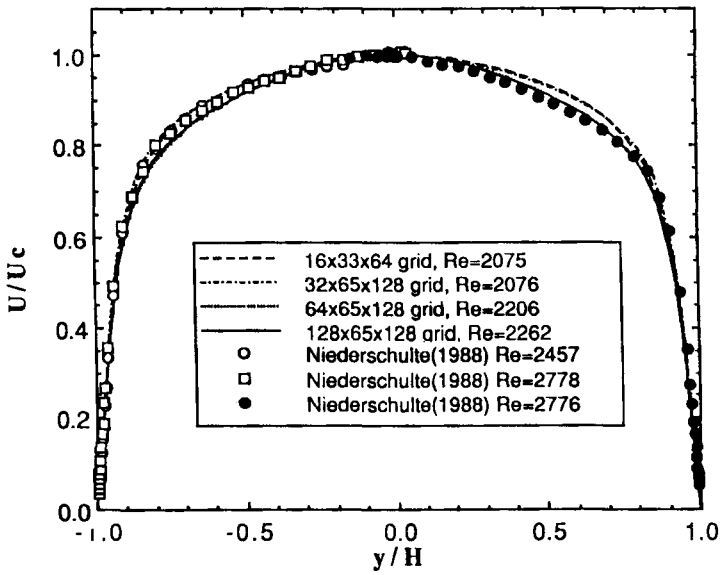

Figure 2. Mean velocity profiles across the channel

$N_x \times N_y \times N_z$. Grids B, C and D show the effect of streamwise resolution. For comparison purposes experimental data for the streamwise and normal velocity components from Niederschulte[16] and experimental data for the spanwise velocity component from Kreplin and Eckelmann[26] are presented in the figures.

The mean velocity is presented in Figures 2 and 3. Figure 2 presents the mean velocity normalized by the centreline velocity versus the co-ordinate y/H. The profiles for grids A and B are flatter than those for grids C and D. This is due to the lower centreline velocity obtained using grids A and B. The profile for grid D is in good agreement with the experimental profiles of Niederschulte and is symmetric about the channel centreline. His profiles had a ratio of the mean centreline velocity to the mean bulk velocity, U_c/U_b, of 1·16 and the simulated profile has a ratio of $U_c/U_b = 1{\cdot}18$. The skin friction coefficient $2\tau_w/(\rho U_b^2)$ predicted by the simulation is 0·00879 compared to 0·00832 from Niedershulte's run at $Re = 2457$. Figure 3 presents the mean velocity profile in wall co-lordinates for the viscous wall region. All four grids correctly give the viscous sublayer region where $U^+ = y^+$ for $y^+ < 7$, but give different results for the buffer region leading into the outer flow region. The profiles increase as the grid resolution increases. It is quite clear that increasing the resolution in the streamwise direction (from $\Delta x = 90{\cdot}5$ to $\Delta x = 22{\cdot}4$) increases the velocity in the outer flow region. It is not clear that the mean velocity has converged as a

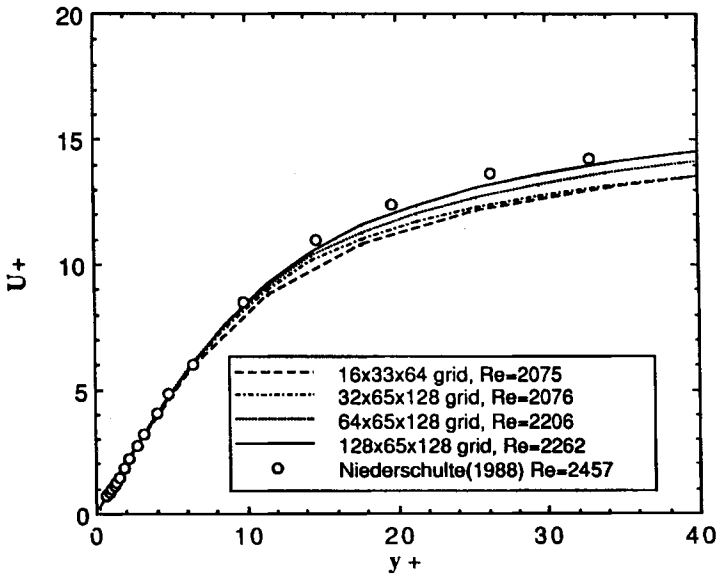

Figure 3. Mean velocity profiles in the viscous wall region

function of grid resolution, though the profile for grid D has converged to that given by the experimental data.

Figures 4 and 5 present the root mean square of the turbulent velocity fluctuations. The streamwise and normal intensities in wall units are presented in Figure 4 and the spanwise intensity is presented in Figure 5. The results for the streamwise intensity varied on all four grids. The streamwise intensity predicted by grid A is higher than that predicted on the other three grids throughout the entire channel. A peak value of 2·84 is obtained at $y^+ = 11{\cdot}4$ on grid A. Grids B, C and D predict peak values of 2·45, 2·41 and 2.56 at $y^+ = 14{\cdot}4$. The streamwise intensities for grids C and D agree for $y^+ > 35$ and are higher than that for grid B. It is not clear that the peak streamwise intensity has converged, but the location of the peak streamwise intensity appears to have converged to $y^+ = 14{\cdot}4$. The normal intensity has clearly converged as a function of grid resolution. The normal intensity predicted by grid A is lower than that by grids B, C and D, which agree. The peak normal intensity on grid A is only 0·702 at $y^+ = 66{\cdot}7$, while those predicted by grids B, C and D are 0·792, 0·812 and 0·792 at $y^+ = 49{\cdot}3$. The spanwise intensity predicted by grid A is also lower than that predicted by the higher-resolution grids. The value and location of the peak spanwise intensity vary on all four grids, so that it appears the solution of the spanwise intensity has not converged as a function of grid resolution. The values of the peak spanwise intensity and their locations of grids A, B, C and D are 0·987 at $y^+ = 25{\cdot}3$, 1·055 at $y^+ = 25{\cdot}3$, 1·058 at $y^+ = 29{\cdot}5$ and 1·039 at $y^+ = 34{\cdot}0$.

The normal intensity profile agrees remarkably well with the experimental data. The experimental results for both the streamwise the spanwise intensities are higher than that predicted by the simulation. The shape of the streamwise intensity profile agrees with the experimental results, including the location of the maximum, $y^+ \approx 14$. The spanwise intensities of Kreplin and Eckelmann measured by hot film anemometry are much higher than the simulation profile in the viscous wall region. Perry *et al.*[27] have determined that most of the data obtained in the near-wall region by standard double-wire techniques may contain significant error caused by cross-contamination. This error would result in higher measured values for the normal and spanwise

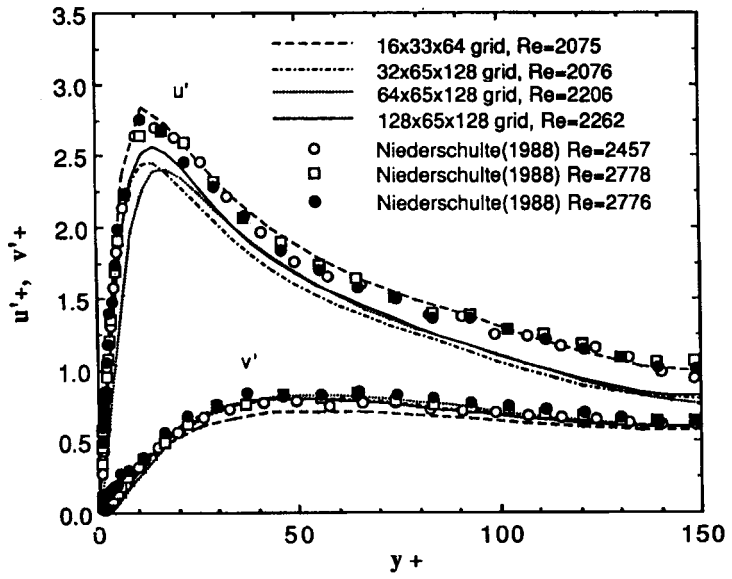

Figure 4. Streamwise and normal intensity profiles

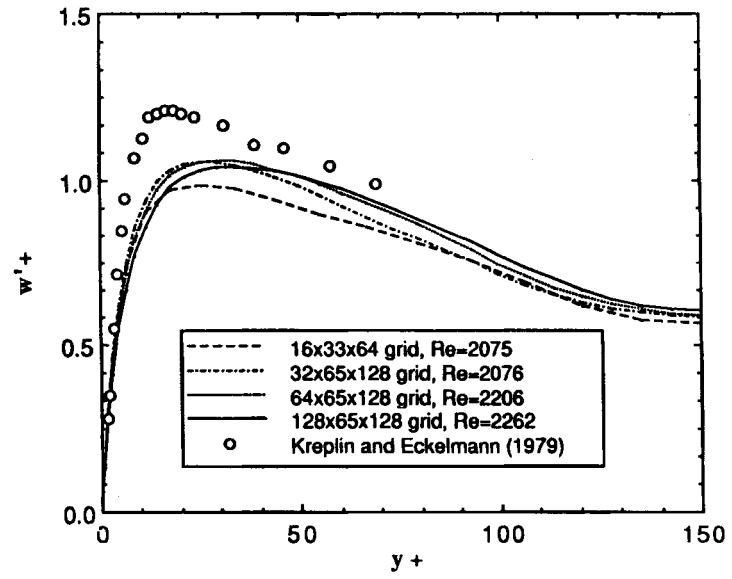

Figure 5. Spanwise intensity profiles

velocity components. Another possible explanation for the differences is that a secondary flow existed in the laboratory channel.

The Reynolds stress term normalized with wall parameters is presented in Figure 6. The profiles for grids A, B and C agree for $y^+ < 70$. The peak value of grid D is lower compared to grids A, B and C. The peak values of the Reynolds stress and their locations for grids A, B, C and

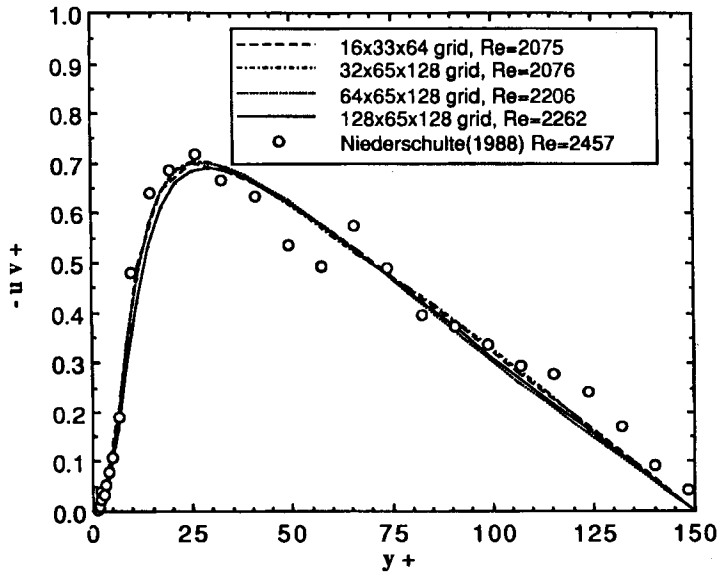

Figure 6. Reynolds stress profiles

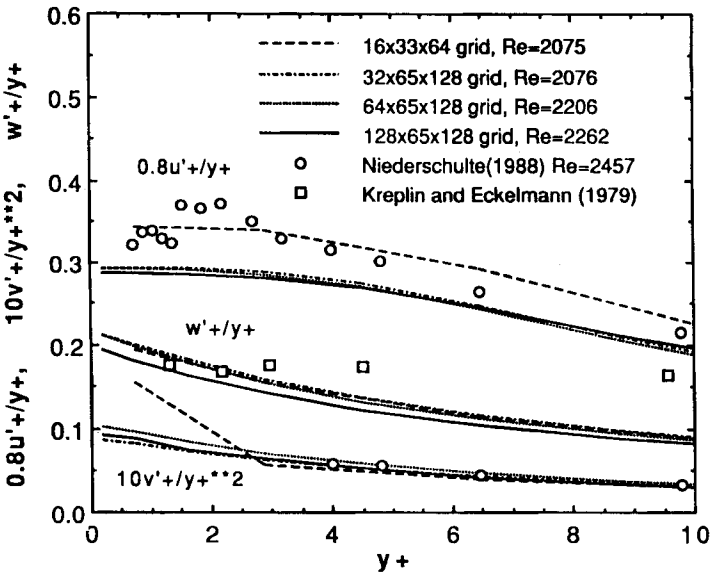

Figure 7. Wall behaviour of the turbulence intensities

D are 0·701 at $y^+ = 25{\cdot}3$, 0·703 at $y^+ = 29{\cdot}5$, 0·701 at $y^+ = 29{\cdot}5$ and 0·691 at $y^+ = 29{\cdot}5$. The profile for grid D shows the correct linear shape in the outer region, indicating that the Reynolds stress has converged. The experimental results are slightly higher than the simulation results towards the channel centre, $H^+ = 150$, since the experiment was done at higher Reynolds number.

Figure 7 shows the limiting behaviour at the wall for the turbulence intensities. The y^+-behaviour of the streamwise and spanwise intensities and the y^{+2}-behaviour of the normal

intensity are expected from the no-slip boundary condition and the continuity equation. The limiting behaviour for the streamwise intensity converged to $0{\cdot}358y^+$ at the wall. The limiting behaviour predicted by grid A is much higher, $0{\cdot}429y^+$. The limiting behaviour for the normal intensity converged to $0{\cdot}00929y^{+2}$ at the wall. The limiting behaviour predicted by grid A is clearly incorrect. This shows that 33 points in the normal direction are not enough to resolve the behaviour of the normal turbulent component at the wall. The normal grid spacing at the wall was only 0·72 for grid A compared to 0·18 for grids B, C and D. The limiting behaviour of the spanwise intensity at the wall converged to $0{\cdot}193y^+$, a much lower value than predicted by grids A, B and C.

Higher-order statistics were also computed and are compared with experimental measurements in Figures 8–11. Figure 8 shows the third-order moments (skewness or kortosis) of the streamwise and normal components of the fluctuating velocity, and Figures 9–11 show the fourth-order moments (flatness) of the streamwise, normal and spanwise fluctuating velocity components. The spanwise skewness is zero for fully developed turbulent channel flow. The experimental measurements of the streamwise and normal skewnesses shown in Figure 8 are significantly different from the Gaussian value of zero. The data have some scatter but the agreement with the computation is quite good (particularly in describing the locations of the zero crossings) over most of the channel. However, close to the wall the experimental data do not show the local minimum in the normal skewness that the simulation gives at $y^+ \approx 12$ and there is too much scatter in the measured streamwise skewness at the wall to make a comparison. The streamwise skewness in the centre of the channel and at the wall dropped as the grid resolution increased. The wall values for grids A, B, C and D are 1·24, 1·05, 1·01 and 0·919. The normal skewness increased for $y^+ > 30$ as the resolution increased. The maximum values and their locations for grids A, B, C and D are 0·297 at $y^+ = 106{\cdot}5$, 0·349 at $y^+ = 106{\cdot}5$, 0·395 at $y^+ = 99{\cdot}5$ and 0·441 at $y^+ = 92{\cdot}6$. The limiting behaviour at the wall was incorrectly predicted on grid A. The wall values for grids B, C and D are −0·143, 0·00811 and 0·419.

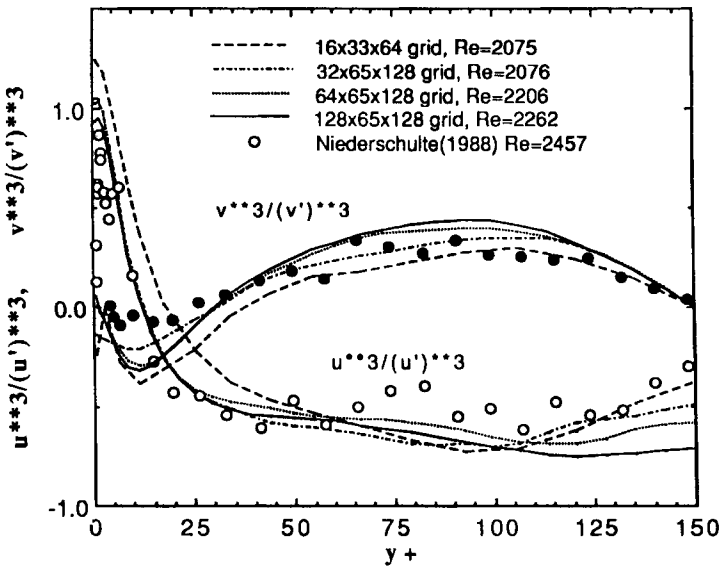

Figure 8. Streamwise and normal skewness profiles

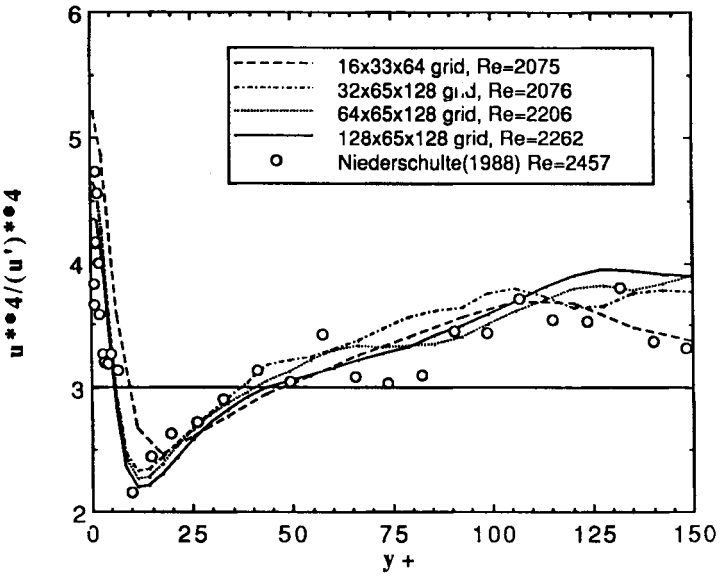

Figure 9. Streamwise flatness profiles

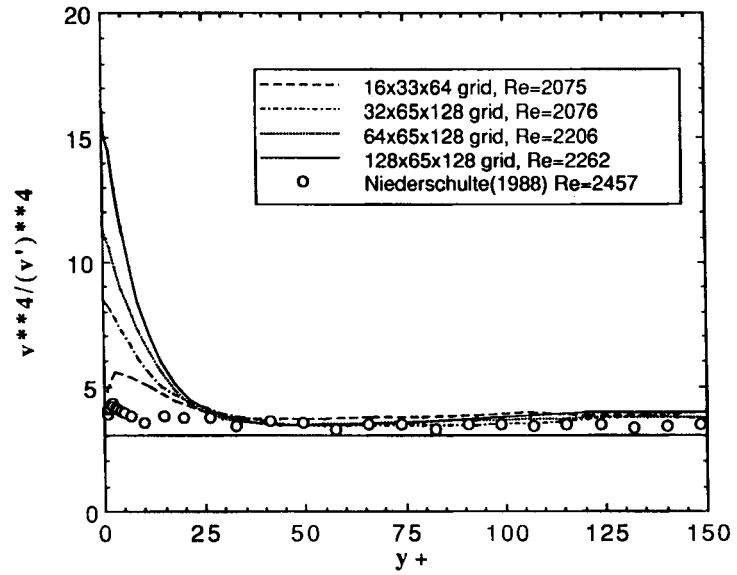

Figure 10. Normal flatness profiles

The calculated flatness profiles are compared with experimental data in Figures 9–11. Note that they are significantly different from the Gaussian value of three. The profile calculated for all grids agree fairly well, except at the wall. The streamwise flatness decreased at the wall as the resolution increased. The wall values of the streamwise flatness for grids A, B, C and D are 5·22, 4·62, 4·52 and 4·32. The normal flatness increased dramatically at the wall as the resolution

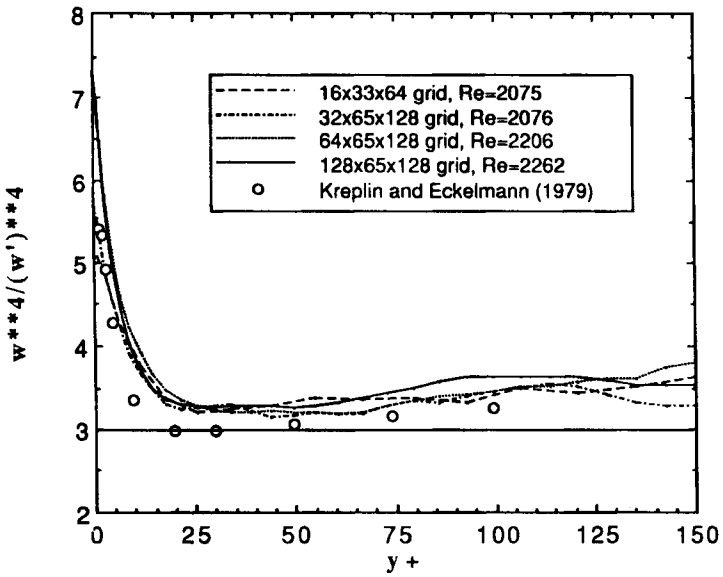

Figure 11. Spanwise flatness profiles

increased. The wall values of the normal flatness for grids A, B, C and D are 4·78, 8·47, 11·5 and 16·5. The simulation of Kim *et al.*[12] gave a value of the normal flatness at the wall of 22. The spanwise flatness at the wall also increased as the resolution increased. The values of the spanwise flatness at the wall for grids A, B, C and D are 5·07, 5·71, 7·25 and 7·32. The spanwise velocity exhibits a near-Gaussian behaviour for $y^+ > 20$ and then climbs rapidly to an asymptote at 7·3 at the wall. This follows the trend of the experimental results and also agrees with the results of Kim *et al.*

The steady state temperature statistics obtained on the four grids are presented in Figures 12–16. For comparison purposes the experimental data of Page *et al.*[18,19] are also presented in the figures (referred to as 'Sage run x').

The mean temperature made dimensionless with the wall temperature and heat flux profiles are presented in Figure 12. The heat flux is constant across the channel. The heat flux did not reach a steady state on grid A and was close to steady state on grid B. The temperature profiles for grids A and B are quite different from those for grids C and D (which agree fairly well) in that they have a larger slope near the wall and are flatter through the core of the channel. The mean temperature profile for grid D is in fairly good agreement with the results of Page *et al.*[18] at the bottom wall and, unlike the experimental data, is symmetric when rotated 180° about the channel centreline. It appears that the temperature profile converged, though it is not clear that the heat flux converged (see Table III).

Figure 13 presents the mean temperature normalized with wall parameters. The computations with different grids agree at the wall but differ in the centre of the channel. This is because the value of the heat flux is still varying with grid resolution. The Nusselt number of 25·36 predicted by the simulation on grid D is in excellent agreement with the data obtained at Reynolds numbers equal to 2340 and 2245. Page *et al.*'s data[18] from both sides of the channel are shown in Figure 13. The agreement of the calculations with grid D and data from runs 45 and 46 is good for $y^+ > 30$. The disagreement with run 40 is due to a Reynolds number effect, since this experiment was

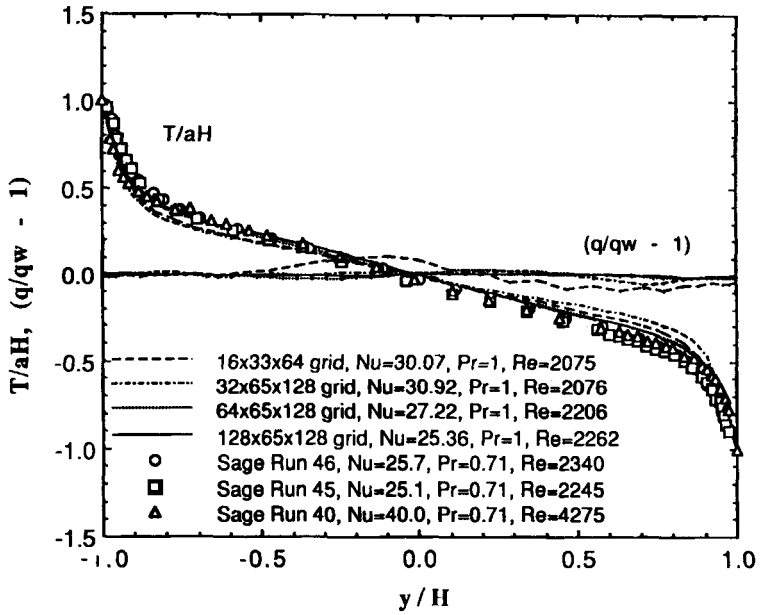

Figure 12. Mean temperature and heat flux profiles across the channel

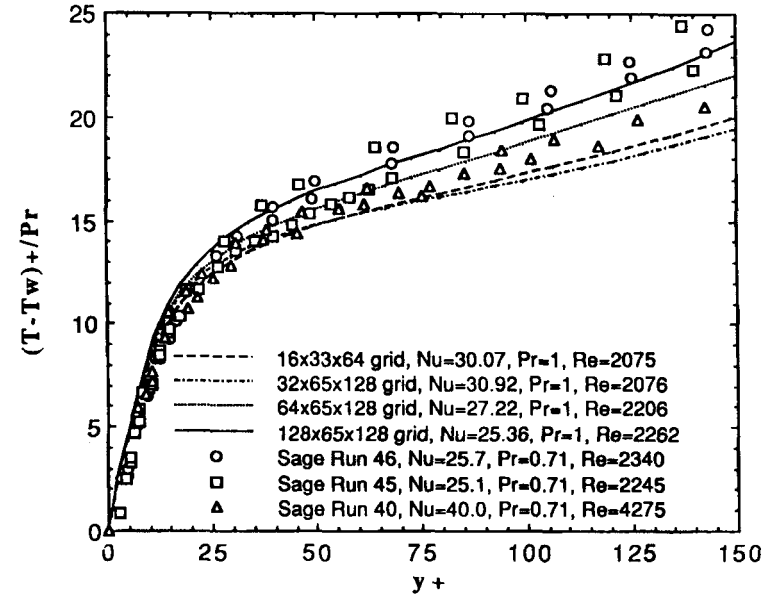

Figure 13. Mean temperature profiles

performed at a Reynolds number twice that of the simulation. A conduction region has to exist close to the wall where the ordinates and abscissae are equal. The computations predict this behaviour for $y^+ < 5$. The experimental data are wrong in this region. This may indicate that the measurement of the total heat flux or of the wall temperature was too high.

Figure 14 presents the eddy conductivity normalized by the half-channel height and the skin friction velocity, where Ec is defined as

$$Ec = \frac{\overline{tv}}{(dT/dy)}. \tag{82}$$

The profiles are not smooth or symmetric, because the numbers of samples in the averages were inadequate and because the temperature field had not reached a steady state on grids A and B. All the eddy conductivity profiles, however, do have the correct shape. The centreline eddy conductivity dropped from 0·121 on grid A to 0·0728 on grid D and the maximum eddy conductivity at $y/H \approx 0{\cdot}5$ converged to approximately 0·095. The profile for run D agrees fairly well with the experimental data of Page *et al.*[19] in the viscous wall region but falls below the experimental data in the channel core. Page *et al.* computed the eddy conductivity by subtracting the molecular conductivity from the total heat flux, not by measuring the temperature–normal velocity correlation. If their heat flux was incorrectly measured and was high, as indicated by Figure 13, then that would explain why their eddy conductivities are higher than that predicted by the simulation. Johnk and Hanratty[28] reported $(Ec+k)/au^* \approx 0{\cdot}081$ near the centre of a pipe for the fully developed heat transfer region. This is in good agreement with the channel core values predicted by the simulation.

Figure 15 presents the calculated results of the root mean square of the temperature fluctuation normalized with wall parameters. Unlike the velocity intensities, the temperature intensities do not decrease in the channel core but reach a maximum at the channel centreline. This arises

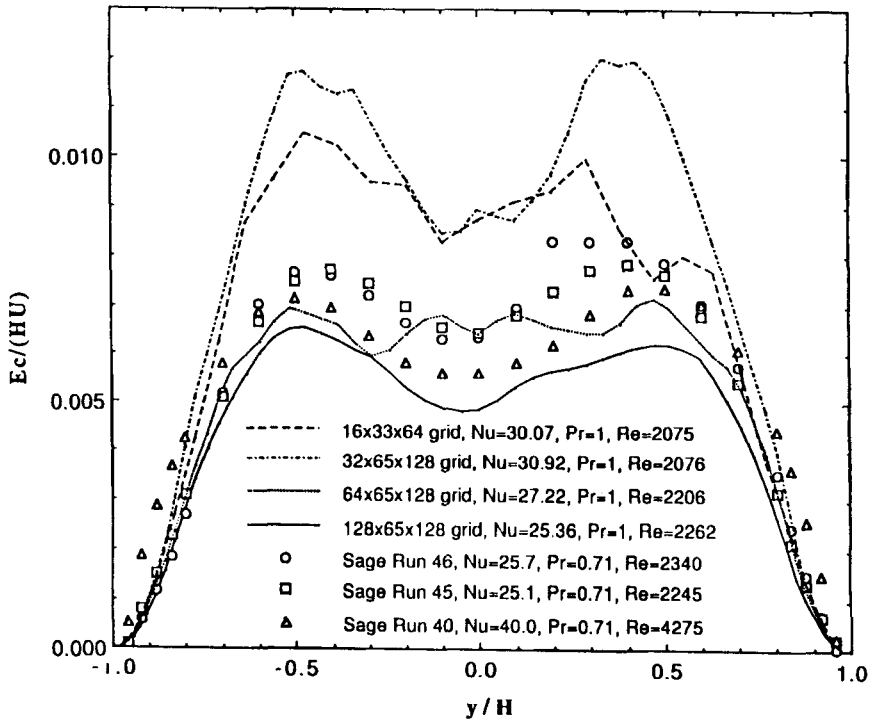

Figure 14. Eddy conductivity profiles

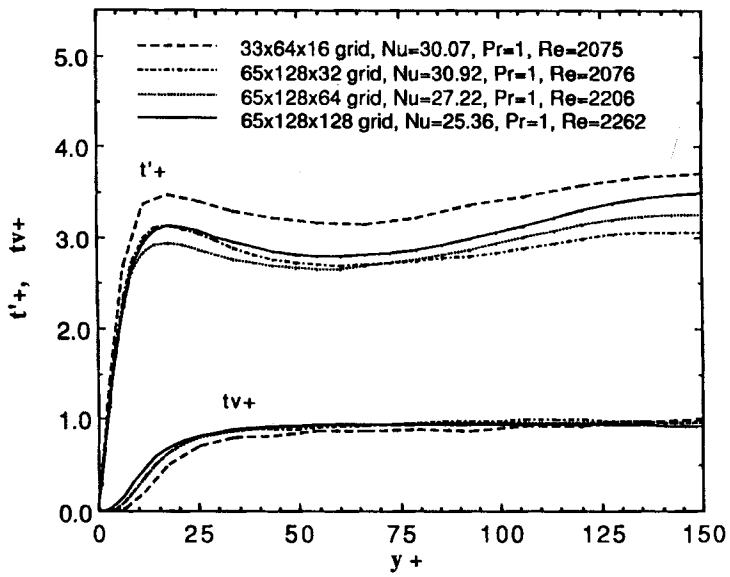

Figure 15. Temperature intensity and temperature–velocity correlation profiles

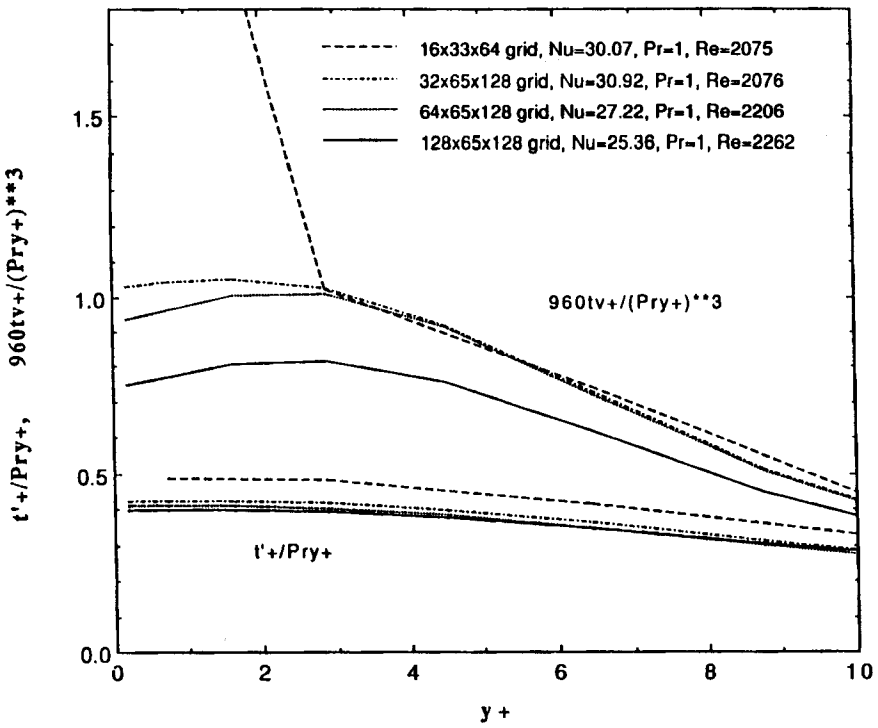

Figure 16. Wall behaviour of the temperature intensity and temperature–velocity correlation

because the different boundary conditions imposed on the temperature and velocity fields at the walls cause a large temperature gradient but a very small velocity gradient in the channel core. There is a local maximum in the temperature intensity in the viscous wall region at $y^+ \approx 17$ which is to be compared with the maximum in the streamwise velocity intensity which occurs at $y^+ \approx 14$. The temperature intensities obtained with grid A are significantly larger than for the other three grids. The results for grids C and D are different because of the different values of the wall heat flux used in the normalization. The peak values of the temperature intensity in the buffer region for grids A, B, C and D are 3·47, 3·13, 2·94 and 3·13 at $y^+ = 17{\cdot}7$. The values of the centreline temperature intensity for grids A, B, C and D are 3·71, 3·06, 3·26 and 3·49.

Figure 15 also presents the temperature–velocity correlation normalized with wall parameters. Grids A and B were not at steady state. Grids C and D have converged and show the proper behaviour, reaching a near-constant value of 0·95 in the outer flow region.

Figure 16 shows the limiting behaviour at the wall for the temperature intensity and temperature–velocity correlation. The near-wall behaviour for the temperature intensity converged to $0{\cdot}397(Pr)y^+$. The near-wall behaviour for the temperature–velocity correlation is incorrectly predicted on grid A owing to its inability to resolve the near-wall normal velocity (see Figure 7). The near-wall behaviour for the temperature–velocity correlation converged to about $0{\cdot}000775[(Pr)y^+]^3$.

7. CONCLUSIONS

A computer programme which combines the Orszag–Kells[7] time-splitting algorithm and the Marcus[9] viscous correction has been developed to simulate the time-dependent three-dimensional turbulent velocity field for fully developed flow in a channel at low Reynolds number. In addition, a fractional time step method developed by Circelli and McLaughlin[14] is used in conjunction with the velocity code to calculate the three-dimensional time-dependent temperature field when heat is being transferred from one wall of the channel to the other.

Statistical properties of the turbulence for this flow vary only with distance from the wall and not in the streamwise and spanwise directions. Calculated mean velocities, mean temperatures and moments of the turbulence agree with laboratory measurements by Niederschulte[16] and by Corcoran, Page and co-workers.[17–19] The calculations with different mesh sizes and the comparison with experiment suggest that the computation converged reasonably well with a $128 \times 65 \times 128$ grid. A surprising aspect of these results is that a good approximation to the flow and temperature field is obtained with $64 \times 65 \times 128$ and the $32 \times 65 \times 128$ coarse grids. Some of the differences between the calculated results and the experimental measurements can be ascribed to errors in the measurements. For example, a plot in the form shown in Figure 13 indicates that there was an error in the measurements of the heat transfer rate or the wall temperature. However, it is not clear whether differences in the moments of the turbulent velocity field close to the wall are due to numerical grid effects or measurement errors. A possible source of experimental error is that smoothing operations used by Niederschulte[16] in analysing his laser Doppler signals could have resulted in his missing the intermittancy at the wall suggested by the computed large values of the flatness.

The results presented in this paper show that, in spite of the remarkable improvements in both computer hardware and software over the last decade, there are still unresolved issues surrounding the use of direct numerical simulation as a tool for turbulence research. The simulations are probably most reliable for processes that are not strongly affected by the highly intermittent character of the normal component of the velocity in the viscous sublayer. The use of periodic boundary conditions may also have some influence on the results, since the simulations reveal the

presence of coherent regions of streamwise velocity fluctuations and Reynolds stress that persist from one end of the computational box to the other even though all the two-point correlation functions become negligibly small at streamwise separations less than $950(\lambda_x/2)$.[29] It is an open question whether such coherence may persist over arbitrarily large distances in the downstream direction. It is also conceivable that the periodic boundary conditions may play some role in the large values of the normal flatness factors near the wall by recycling strong disturbances that might otherwise not reappear in a given region for a long period of time. However, these issues will be difficult and expensive to resolve, since one must perform simulations with considerably larger periodicity lengths to assess their influence.

It is interesting and important to note that, with the exception of the normal direction, the grid spacings used in the simulations reported in the present paper are larger than the Kolmogorov length scale. In fact, even on grid D the grid spacing in the streamwise direction is an order of magnitude larger than the Kolmogorov scale. The fact that the simulations reproduce the correct statistical behaviour, at least for low-order moments, suggests that the neglected length scales are unimportant except possibly for disturbances which are statistically unlikely. This result is fortunate, since even with the most powerful present-day computers it is not feasible to perform simulations of the type discussed in the present paper in which the grid spacings are all smaller than the Kolmogorov scale and, at the same time, all of the large scales in the flow are correctly described.

The heat transfer simulations reported in this paper are an example of the kind of use for which direct numerical simulation can provide valuable information that would be very difficult to obtain with existing experimental techniques. Direct simulation, for example, allows one to construct a detailed energy balance in order to determine the relative importance of various transport processes.[30] The corresponding laboratory measurements are, in principle, feasible, but formidable in practice. Lagrangian particle-tracking experiments are another example of how direct simulation can provide valuable information that is otherwise difficult to obtain. The results of such a study for aerosol particles were recently reported by one of us.[31]

ACKNOWLEDGEMENTS

This work was supported by the Fluid Dynamics Program of the Office of Naval Research (Grant N00014-82-K0324) and by the Transport Phenomena Program of the National Science Foundation (Grant NSF-CBT-88-00980). J.B.M. acknowledges support from the Department of Energy under contract DE-FG02-88ER13919. We also acknowledge the support and facilities of the U.S. Army Ballistic Research Laboratory at Aberdeen Proving Grounds, Maryland and the National Center for Supercomputer Applications at the University of Illinois, Urbana.

REFERENCES

1. J. W. Deardorff, 'A numerical study of three-dimensional turbulent channel flow at large Reynolds numbers', *J. Fluid Mech.*, **41**, 453–480 (1970).
2. U. Schumann, 'Ein Verfahren zur direkten numerischen Simulation turbulenter Stroemungen in Platten- und Ringspaltkanaelen und ueber seine Anwendung zur Untersuchung von Turbulenz-modellen', *Dissertation*, University of Karlsruhe, 1973.
3. P. Moin and J. Kim, 'Numerical investigation of turbulent channel flow', *J. Fluid Mech.*, **118**, 341–377 (1982).
4. D. T. Hatziavramidis and T. J. Hanratty, 'The representation of the viscous wall region by a regular eddy pattern', *J. Fluid Mech.*, **95**, 655–679 (1979).
5. D. R. Chapman and G. D. Kuhn, 'Two-component Navier–Stokes computational model of viscous sublayer turbulence', *AIAA Paper 81-1024*, 1981.
6. S. L. Lyons, C. Nikolaides and T. J. Hanratty, 'The size of turbulent eddies close to a wall', *AIChE J.*, **34**, 938–945 (1988).

7. S. A. Orszag and L. C. Kells, 'Transition to turbulence in plane Poiseuille and plane Couette flow', *J. Fluid Mech.*, **96,** 159–205 (1980).
8. S. A. Orszag and A. T. Patera, 'Secondary instability of wall-bounded shear flows', *J. Fluid Mech.*, **128,** 347–385 (1983).
9. P. S. Marcus, 'Simulation of Taylor–Couette flow', *J. Fluid Mech.*, **146,** 45–64 (1984).
10. R. D. Moser and P. Moin, 'Direct numerical simulation of curved turbulent channel flow', *NASA TM 85974*, 1984.
11. P. R. Spalart, 'Numerical study of sink-flow boundary layers', *J. Fluid Mech.*, **172,** 307–328 (1986).
12. J. Kim, P. Moin and R. Moser, 'Turbulence statistics in fully developed channel flow at low Reynolds number', *J. Fluid Mech.*, **177,** 133–166 (1987).
13. A. Leonard and A. Wray, 'A new numerical method for simulation of three-dimensional flow in a pipe', in E. Krause (ed.), *Proc. 8th Int. Conf. on Numerical Methods in Fluid Dynamics*, Lecture Notes in Physics, vol. 170, Springer, New York, 1982, pp. 335–342.
14. B. R. Circelli and J. B. McLaughlin', A numerical study of heat transfer in turbulent shear flow', *Numer. Heat Transfer*, **9,** 335–348 (1986).
15. S. L. Lyons, 'A direct numerical simulation of fully developed turbulent channel flow with passive heat transfer', *Ph.D. Dissertation*, University of Illinois, Urbana, 1989.
16. M. A. Niederschulte, 'Turbulent flow through a rectangular channel', *Ph.D. Dissertation*, University of Illinois, Urbana, 1988.
17. W. H. Corcoran, F. Page Jr., W. G. Schlinger and B. H. Sage, 'Methods and apparatus for flow between parallel plates', *Ind. Eng. Chem.*, **44,** 410–419 (1952).
18. F. Page Jr., W. H. Corcoran, W. G. Schlinger and B. H. Sage, 'Temperature and velocity distributions in uniform flow between parallel plates', *Ind. Eng. Chem.*, **44,** 419–424 (1952).
19. F. Page Jr., W. G. Schlinger, D. K. Breaux and B. H. Sage, 'Point values of eddy conductivity and viscosity in uniform flow between parallel plates', *Ind. Eng. Chem.*, **44,** 424–430 (1952).
20. S. A. Orszag, 'Numerical simulation of incompressible flows within simple boundaries: accuracy', *J. Fluid Mech.*, **49,** 75–112 (1971).
21. P. M. Gresho, 'On the theory of semi-implicit projection methods for viscous incompressible flow and its implementation via a finite element method that also introduces a nearly-consistent mass matrix', *Int. j. numer methods fluids*, **11,** 587–620 (1990).
22. P. M. Gresho and R. L. Sani, 'On pressure boundary conditions for the incompressible Navier–Stokes equations', *Int. j. numer. methods fluids*, **7,** 1111–1145 (1987).
23. D. Gottlieb and S. A. Orszag, 'Numerical analysis of spectral methods: theory and applications', *CBMS–NSF Monograph 26*, SIAM, Philadelphia, 1977.
24. S. A. Orszag, 'Numerical simulation of incompressible flows within simple boundaries', *Stud. Appl. Math.*, **L,** 293–327 (1971).
25. S. A. Orszag, 'On the elimination of aliasing in finite-difference schemes by filtering high-wavenumber components', *J. Atmos. Sci.*, **28,** 1074 (1971).
26. H. Kreplin and H. Eckelmann, 'Behavior of the three fluctuating velocity components in the wall region of a turbulent channel flow', *Phys. Fluids*, **22,** 1233–1239 (1979).
27. A. E. Perry, K. L. Lim and S. M. Henbest, 'A spectral analysis of smooth flat-plate boundary layers', in J. Lumley (ed.), *Proc. 5th Symp. on Turbulent Shear Flows*, Cornell University, New York, 1985, pp. 9.29–9.34.
28. R. E. Johnk and T. J. Hanratty, 'Temperature profiles for turbulent flow of air in a pipe', *Chem. Eng. Sci.*, **17,** 867–879 (1962).
29. S. L. Lyons, T. J. Hanratty and J. B. McLaughlin, 'Turbulence-producing eddies in the viscous wall region', *AIChE J.*, **35,** 1962–1974 (1989).
30. S. L. Lyons, T. J. Hanratty and J. B. McLaughlin, 'Direct numerical simulation of passive heat transfer in a turbulent channel flow', *Int. J. Heat Mass Transfer*, **34,** 1149–1162 (1991).
31. J. B. McLaughlin, 'Aerosol particle deposition in numerically simulated channel flow', *Phys. Fluids A*, **1,** 1211–1224 (1989).